PAPER

Check for updates

Multipole-moment effects in ion–molecule reactions at low temperatures: part III – the He+ + CH4 and He+ + CD4 reactions at low collision energies and the effect of the charge-octupole interaction

Valentina Zhelyazkova, [iD] Fernanda B. V. Martins [iD] and Frédéric Merkt [iD] *

We present experimental and theoretical studies of the $He^+ + CH_4$ and $He^+ + CD_4$ reactions at collision energies in the $k_B \cdot (0-10)$ K range. Helium atoms in a supersonic beam are excited to a low-field-seeking Rydberg–Stark state and merged with a supersonic beam of CH_4 or CD_4 using a curved surface-electrode deflector. The ion–molecule reactions are studied within the orbit of the helium Rydberg [He(n)] electron, which suppresses stray-electric-fields-induced heating and makes it possible to reach very low collision energies. The collision energy is varied by adjusting the velocity of the He(n) atoms with the surface deflector, keeping the velocity of the methane beam constant. The reaction product ions $(C(H/D)_p^+$ with $p \in \{1,2,3\})$ are collected in a time-of-flight mass spectrometer and monitored as a function of the collision energy. No significant energy-dependence of the total reaction yields of either reactions is observed. The measured relative reaction rate coefficient for the $He^+ + CH_4$ reaction is approximately twice higher than the one for the $He^+ + CD_4$ reaction. The CH^+, CH_2^+ and CH_3^+ (CD^+, CD_2^+ and CD_3^+) ions were detected in ratios $0.28(\pm 0.04):1.00(\pm 0.11):0.11(\pm 0.04)$ $[0.35(\pm 0.07):1.00(\pm 0.16):0.04_{-0.04}^{+0.09}]$. We also present calculations of the capture rate coefficients for the two reactions, in which the interaction between the charge of the helium ion and the octupole moment of the methane molecule is included. The rotational-state-specific capture rate coefficients are calculated for states with $J = (0-3)$ at collision energies below $k_B \cdot 15$ K. After averaging over the rotational states of methane populated at the rotational temperature of the supersonic beam, the calculations only predict extremely weak enhancements (in the order of $\sim 0.4\%$) of the rate coefficients compared to the Langevin rate constant k_L over the collision-energy range considered.

1 Introduction

Numerous ion–molecule reactions are barrierless and exothermic and proceed with high rate coefficients even at very low temperatures. These reactions play an important role in the chemistry of the tenuous (with number density $<10^6$ cm^{-3})[1] and cold (10–150 K) environment of interstellar clouds.[2] Precise knowledge of the absolute reaction rate coefficients and the branching ratios for different product channels is necessary as input parameters for kinetics models of the relevant chemical processes.[1,3–5] Ion–molecule reactions at and above room temperature have been experimentally studied since the 1960s in drift-tube,[6] flowing-afterglow,[7] selected ion-flow tube[8] and ion-cyclotron-resonance[9] setups. The introduction of the uniform-supersonic-flow method to study ion–molecule reactions in the 1980s made it possible to

reach temperatures down to ≈ 10 K.[10] Such low temperatures can also be reached in experiments with sympathetically cooled ions in ion traps and guided ion beams.[11–13] In recent years, techniques relying on the combination of trapped ions in Coulomb crystals and slow beams of molecules have been developed to study low-temperature ion–molecule chemistry.[14,15]

In most experiments, stray electric fields in the reaction volume accelerate the ions, which prevents investigations below ~ 10 K. This limitation is unfortunate, because it is precisely below 10 K that strong variations of the rate coefficients with the temperature or the collision energy are expected.[16–24] Replacing the ion with an atom or molecule in a Rydberg state and merging the Rydberg sample with a supersonic beam containing the molecule of interest suppresses the heating of the ion core by stray electric fields and enables one to reach very low collision energies, down to $\sim k_B \cdot 100$ mK,[25–30] when studying the reactions within the Rydberg-electron orbit.

ETH Zurich, Zurich, Switzerland. E-mail: merkt@phys.chem.ethz.ch

This article is the third in a series of three articles exploring the effect of the molecular electric multipole moments on ion–molecule reaction rate coefficients at low collision energies. The article series is dedicated to studies of the interactions between the He^+ ion and molecules possessing either a dipole, a quadrupole or an octupole moment. In the series, we also develop and test the theoretical framework necessary for treating the ion-multipole-moment interactions and calculating the rotational-state-dependent capture rate coefficients at low collision energies. Experimentally, we reach collision energies close to 0 K in a merged-beam approach by replacing the He^+ ion with a helium atom in a Rydberg state (referred to as $He(n)$ henceforth). We vary the energy of the collision by varying the velocity of the $He(n)$ atoms using a surface-electrode Rydberg–Stark deflector,[27,29–31] and keeping the velocity of the molecular beam fixed.

In the first article of this series (Article I),[29] the reaction between He^+ and ammonia (both NH_3 and ND_3) was investigated in the $k_B \cdot (0–40)$ K collision-energy range to characterise the effect of the charge–dipole interaction. A significant increase of the total reaction yield at the lowest collision energies was observed and attributed to the interaction between the dipole of the ammonia molecule and the He^+-ion charge. In the second article (Article II),[32] the $He^+ + N_2$ reaction was studied in the range of collision energies between 0 and $k_B \cdot 10$ K and a suppression of $\sim 30\%$ of the reaction yield was observed at the lowest collision energies compared to the reaction yield at $E_{coll}/k_B \approx 10$ K. This suppression was attributed to the interaction between the negative quadrupole moment (Q_{zz}) of the N_2 molecule and the He^+ ion charge. In the current article, we extend these studies to reactions involving molecules that do not have a permanent dipole or quadrupole moment and present results on the $He^+ + CH_4$ and $He^+ + CD_4$ reactions in the $k_B \cdot (0–10)$ K collision-energy range.
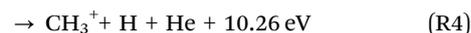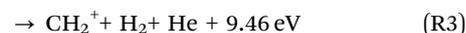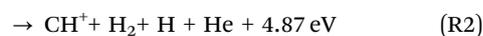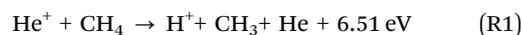
The lowest nonvanishing electric moment of methane is the octupole moment ($\Omega_{CH4} = 3.12\ ea_0^3$).[33] Interactions between oriented (in the case of the dipole) and aligned (in the case of the quadrupole) molecules and ions scale with the ion–molecule separation R as R^{-2} and R^{-3}, respectively. In the case of the octupole moment the interaction scales as R^{-4}. Because of the small value of Ω_{CH4} and the $R^{-4}-$ dependence of the charge-octupole-moment interaction, the reaction between methane and the helium ion is expected to be well described by the Langevin capture model down to very low collision energies. Our experiments are carried out to test this expectation. To complement the experimental observations, we present theoretical calculations of the rotational-state-dependent capture rate coefficients for the $He^+ + CH_4$ and $He^+ + CD_4$ reactions.

The current paper is organised as follows. After a short introduction to the $He^+ + CH_4$ reaction in the remainder of this introductory section, we briefly recapitulate the main aspects of the experimental setup and method in Section 2. The experimental results are then reported in Section 3. In Section 4, we present calculations of the rotational-state-dependent reaction rate coefficients for the rotational states of methane that are populated at the 6 K rotational temperature

of the supersonic source ($J \leq 2$). Finally, we present the conclusions for this article and the three-article series in Section 5.

The reactions between He^+ and methane at low temperatures and densities have relevance for the chemistry of the interstellar medium (ISM). Methane has been detected both in the gas phase and as ice in several interstellar molecular clouds,[34] with an abundance estimated to be $\sim 10^{-3}$ that of carbon monoxide, the second most abundant molecule in the ISM after H_2.[35] Helium is the second most abundant species in the ISM, corresponding to about 25% of the primordial baryonic mass of the universe,[36] and it can be ionised by cosmic rays to form He^+.[2] The ionisation energy of ^4He (24.5874 eV)[37] is higher than that of all neutral atomic and molecular species, and in particular much higher than the adiabatic ionization energy of CH_4 (12.615 eV),[38] and even higher than the dissociative ionisation energy of CH_4.[39]

The reaction between methane and He^+ has been studied at ~ 300 K and ~ 700 K in the 1970s and 1980s in drift-tube (DT),[40] ion-cyclotron-resonance (ICR),[41,42] selected-ion-flow-tube (SIFT)[43] and flowing-afterglow (FA)[44] experiments, and in the 2000s at higher collision energies in the 4–4000 eV range.[45] The main reaction channels observed in several of the experiments conducted at 300 and 700 K are:

$$He^+ + CH_4 \rightarrow H^+ + CH_3 + He + 6.51\ eV \quad (R1)$$

$$\rightarrow CH^+ + H_2 + H + He + 4.87\ eV \quad (R2)$$

$$\rightarrow CH_2^+ + H_2 + He + 9.46\ eV \quad (R3)$$

$$\rightarrow CH_3^+ + H + He + 10.26\ eV \quad (R4)$$

$$\rightarrow CH_4^+ + He + 11.97\ eV, \quad (R5)$$

and the product-ion distributions measured in ref. 40–43 are summarised in Table 1. Other energetically allowed reaction channels, e.g., those leading to the formation of H_2^+, H_3^+, HeH^+ and C^+ ions, were not detected so far and are expected not to be significant at low energies.[43] The total reaction rate coefficient in these experiments was found to be in the $[1.25(\pm 0.19) - 1.7(\pm 0.34)] \times 10^{-15}\ m^3\ s^{-1}$ range, consistently lower than the Langevin rate constant ($k_L = 2.048 \times 10^{-15}\ m^3\ s^{-1}$). In these studies the dominant product ions were found to be CH_2^+ (50–53%), H^+ (25–28%) and CH^+ (14–16%), with smaller contributions from CH_3^+ (4–5%) and CH_4^+ (1–3%). The H^+ product was not detected in one of the experiments (ref. 41), while in another experiment (ref. 42) it was not directly detected but its production was deduced from the loss of the total ion signal.

Table 1 Distributions of the $He^+ + CH_4$ reaction product ions reported in ref. 40–43

	Ref. 40	Ref. 41	Ref. 43	Ref. 42
	(DT)	(ICR)	(SIFT)	(ICR)
H^+	0.28	—	0.25	0.28
CH^+	0.14	0.19	0.16	0.14
CH_2^+	0.53	0.74	0.53	0.50
CH_3^+	0.04	0.05	0.05	0.05
CH_4^+	0.02	0.03	0.01	0.03

This journal is © the Owner Societies 2022

Phys. Chem. Chem. Phys., 2022, **24**, 16360–16373 | **16361**

This inconsistency regarding the observation of H^+ as a reaction product in the different experiments originates from its high kinetic energy and low mass, which make its detection challenging. In our experiments, we have not observed significant amounts of H^+ product ions and disregard the corresponding reaction channel from our analysis. Consequently, when we use the term branching ratios for given reaction channels, we exclude the contributions leading to H^+ or D^+ products.

2 Experimental setup

The experimental setup has been described in detail in Article I of the current series (see also ref. 27). Here we outline the details relevant to the study of the $He(n) + CH_4$ and $He(n) + CD_4$ reactions.

The merged-beam apparatus consists of two supersonic beams produced by home-built short-pulse valves (pulse duration ~ 20 μs, repetition rate 25 Hz) – one for the He and one for the ground-state (GS) methane beams. The two beams propagate along axes initially separated by a $5°$ angle. An electric discharge at the He valve orifice populates the metastable $(1s)(2s)$ $^3S_1$ state of helium (referred to as He* below). After passing through two skimmers, the He* beam is crossed at right angles by a UV laser beam and is photoexcited in a dc electric field to a low-field-seeking Rydberg–Stark state $[(n, k, m) = (30, 21, 0)$, referred to as $He(n)$ below]. After excitation, the $He(n)$ atoms are loaded into electric quadrupole traps formed above the surface of the 50-electrode Rydberg–Stark decelerator and deflected and merged with the GS supersonic beam. After the $He(n)$ atoms are merged with the GS beam, they enter a Wiley–McLaren-type[46] time-of-flight mass spectrometer (TOF-MS), where the reaction product ions are extracted toward a microchannel plate (MCP) detector in a direction perpendicular to the merged-beam propagation axis (see Fig. 1 of Article I). In the experiments described here, the helium valve is temperature-stabilised to 100.0 ± 0.1 K, resulting in a supersonic beam with a mean forward velocity of about 1000 m s^{-1}. By setting the appropriate time-dependent potentials to the electrodes of the surface deflector, the trapped $He(n)$ atoms can also be accelerated or decelerated to selected final velocities, v_{Ryd}, in the 750–1200 m s^{-1} range.

The GS-beam valve has an orifice diameter of ~ 0.5 mm. It is operated with one of the following gases: (i) pure $^{12}CH_4$, (ii) pure $^{12}CD_4$, and (iii) a mixture of $^{13}CH_4$ and $^{12}CD_4$, corresponding to molar fractions of $x(^{13}CH_4) = 0.479$ and $x(^{12}CD_4) = 0.521$, determined from the weight of the gas cylinder before and after filling it with CH_4 and CD_4. For the measurements recorded with gas samples (i) and (ii), the valve was temperature-stabilised to 273 K and the gas was kept at a stagnation pressure of 2.5 bar. The measurements recorded with the $^{13}CH_4$–$^{12}CD_4$ mixture were performed with the valve operated at room temperature and a stagnation pressure of 4 bar. Two fast ionisation gauges (FIGs) positioned after the TOF-MS were used to determine the velocity distribution of the GS beam. The central velocities, v_{GS}, of the $^{12}CH_4$, $^{12}CD_4$ and $^{13}CH_4$–$^{12}CD_4$ mixture beams were measured to be 1068 ± 5 m s^{-1}, 960 ± 5 m s^{-1} and 1033 ± 5 m s^{-1}, respectively.
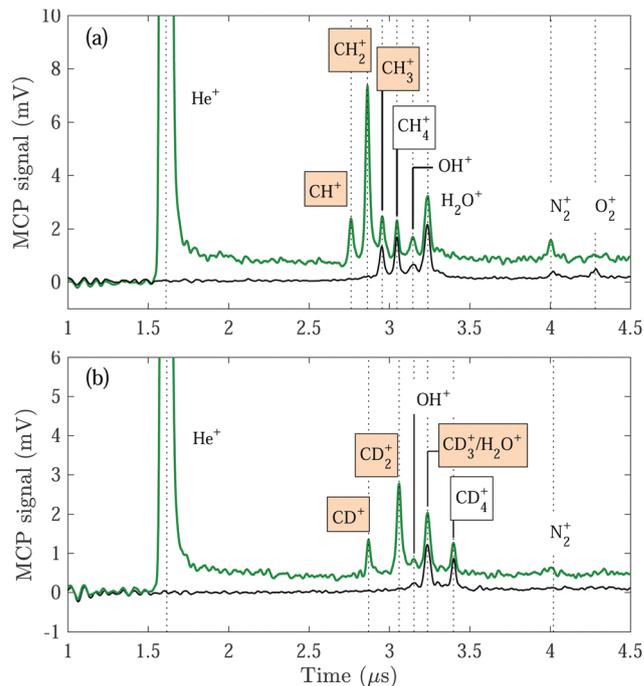
Fig. 1 Product-ion TOF mass spectra recorded following reactions between the $He(n)$ Rydberg atoms and a ground-state beam containing either pure $^{12}CH_4$ (a) or pure $^{12}CD_4$ (b) gas. The green and black traces depict the mass spectra measured with the Rydberg excitation laser turned on and off, respectively. The $He(n)$ mean velocity used to record the spectra shown in both (a) and (b) is $v_{Ryd} = 1040$ m s^{-1}, and the reaction time is $\Delta t_r = 7$ μs. The coloured boxes indicate the detected products ions of the $He^+ + CH_4/CD_4$ reactions.

The reaction product ions were collected by applying a potential of 1 kV (0.5 kV) to electrode E_1 (E_2) [see Fig. 1 of Article I]. A prepulse of 125 V applied to E_1 was used to define a reaction-observation time Δt_r of 7 μs, as explained in Article I.

3 Results

3.1 Ion-product mass spectra and integrated signals

Displayed in Fig. 1 are reaction-product TOF mass spectra measured following reactions between the $He(n)$ atoms and a GS beam containing pure CH_4 (a) and pure CD_4 (b) gas. The spectra were recorded with the $He(n)$ atoms guided by the surface deflector at a constant velocity of $v_{Ryd} = 1040$ m s^{-1}, corresponding to collision energies of $E_{coll}/k_B = 0.2$ K (a) and 1.2 K (b). When the Rydberg-excitation laser is turned on [green traces in Fig. 1(a) and (b)], a prominent peak is visible at ~ 1.6 μs, corresponding to field-ionised helium Rydberg atoms.

In addition, several peaks appear in the TOF mass spectra. These peaks can be assigned to (i) the GS-beam-specific reaction products from reactions (R2), (R3) and (R4), *i.e.*, $CH_{p \in \{1,2,3\}}^+$ (a) and $CD_{p \in \{1,2,3\}}^+$ (b) ions, (ii) ions produced from the Penning-ionisation reactions

$$He^* + CH_4 \rightarrow He + CH_3^+ + H \qquad (R6)$$

$$\rightarrow He + CH_4^+, \qquad (R7)$$

16362 | *Phys. Chem. Chem. Phys.*, 2022, **24**, 16360–16373

This journal is © the Owner Societies 2022

and equivalently for the He* + CD$_4$ reaction, and (iii) ions originating from Penning ionisation of trace amounts of water, oxygen and nitrogen (*e.g.*, OH$^+$, H$_2$O$^+$, N$_2{}^+$ and O$_2{}^+$) present in the vacuum chamber.

To distinguish the ion products formed in the He(n) + CH$_4$/CD$_4$ reactions from ions formed in the Penning-ionisation reactions (R6) and (R7), we also recorded mass spectra with the Rydberg-excitation laser turned off [black traces in 1(a) and (b)]. When the GS beam is CH$_4$, we can identify the He* + CH$_4$ reaction products to be CH$_3{}^+$ and CH$_4{}^+$, in addition to the products originating from reactions with the H$_2$O, N$_2$ and O$_2$ molecules in the reaction chamber. The Penning-ionisation products from the He* +CD$_4$ reaction are analogous to the ones from the He* + CH$_4$ reaction, however, the H$_2$O$^+$ and CD$_3{}^+$ ions both have a mass of ~18 u and are not resolved in the mass spectra.

We did not observe the H$^+$ or D$^+$ product ions in our experiments. For all other product ions, no significant losses are expected to take place during the reaction–observation time. Moreover, the detection efficiency can be assumed to be identical for all reaction product ions because of their similar masses.

A considerable He$^+$ signal is detected even when the GS beam is on, indicating that only a small fraction (about 1%) of the He(n) atoms takes part in the chemical reaction, as already observed for the other reactions discussed in Articles I and II. Because the particle number density of the GS beam is much greater than that of the Rydberg atoms, the reaction can be described with pseudo-first-order kinetics. From the experimental conditions under which the supersonic expansion is produced, we estimate that the density of the GS-beam particles in the interaction region is $\rho_{GS} \approx 3 \times 10^{17}$ m^{-3} using standard expressions for the isentropic expansion of gases in vacuum.[47] The estimated effective reaction rate coefficient is $k_{eff} = k_L\rho_{GS} \approx 6 \times 10^2$ s^{-1}, corresponding to a reaction probability per He(n) atom of only 0.004 during the 7 µs-long reaction–observation time. Typically, less than one reaction product ion is detected on average during each experimental cycle.

We measure the dependence of the product-ion yields of the He$^+$ + CH$_4$ and He$^+$ + CD$_4$ reactions on the collision energy $E_{coll} = \frac{1}{2}\mu v_{rel}{}^2 = \frac{1}{2}\mu(v_{Ryd} - v_{GS})^2$ (μ is the reduced mass) by varying v_{Ryd} and keeping v_{GS} constant. The integrated product-ion signals, $I_{CH_{\{1,2,3\}}^+}$ and $I_{CD_{\{1,2,3\}}^+}$, were corrected for (i) the different amount of He(n) atoms and (ii) the different overlap with the GS beam dependent on v_{Ryd}, as explained in part I. Time-of-flight spectra recorded with the excitation laser turned off are subtracted from each recorded reaction time-of-flight mass spectrum prior to integration. The measured product-ion branching ratios, excluding the contributions from channels releasing H$^+$/D$^+$, for the two reaction systems are summarised in Table 2 in Section 3.2.

3.2 Reaction-product yields as a function of the reaction collision energy

Fig. 2(a) and (b) display the integrated product-ion signals I_{CH^+}, $I_{CH_2^+}$ and $I_{CH_3^+}$ (I_{CD^+}, $I_{CD_2^+}$ and $I_{CD_3^+}$) measured for the He$^+$ + CH$_4$

Table 2 Branching ratios for the formation of the C(H/D)$^+$, C(H/D)$_2{}^+$ and C(H/D)$_3{}^+$ product ions measured in the current work and the relative branching ratios for the CH$^+$, CH$_2{}^+$ and CH$_3{}^+$ product ions measured in ref. 40–43. The branching ratios exclude the contributions from H$^+$ and CH$_4{}^+$ which could not be reliably detected in our experiments

	C(H/D)$^+$	C(H/D)$_2{}^+$	C(H/D)$_3{}^+$
He$^+$ + CH$_4$ (this work)	0.20 ± 0.03	0.72 ± 0.08	0.08 ± 0.03
He$^+$ + CD$_4$ (this work)	0.25 ± 0.05	0.72 ± 0.11	$0.03_{0.03}^{+0.07}$
Ref. 40	0.197	0.746	0.0563
Ref. 41	0.194	0.755	0.0510
Ref. 43	0.216	0.716	0.0676
Ref. 42	0.203	0.725	0.0725
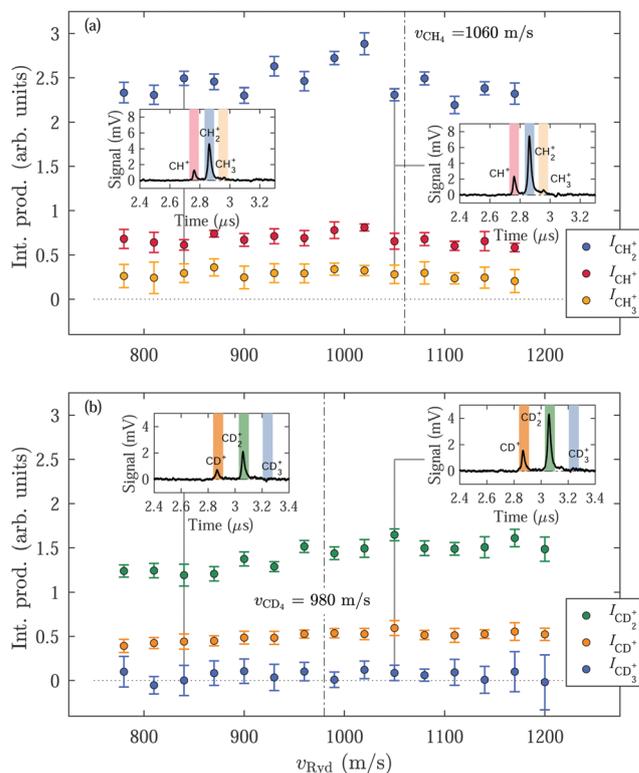
Fig. 2 Measured product-ion yields from the (a) He$^+$ + CH$_4$ and (b) He$^+$ + CD$_4$ reactions, as a function of v_{Ryd}. (a) $I_{CH_2^+}$ (blue circles), I_{CH^+} (red circles) and $I_{CH_3^+}$ (orange circles). (b) $I_{CD_2^+}$ (green circles), I_{CD^+} (orange circles) and $I_{CD_3^+}$ (blue circles). The insets show the TOF spectra recorded for $v_{Ryd} = 840$ and 1050 m s^{-1} (indicated by grey vertical lines), after subtraction of the Penning-ionisation contribution. The dash-dotted vertical lines indicate the selected velocity of the CH$_4$ and CD$_4$ molecules.

and He$^+$ + CD$_4$ reactions, respectively. The error bars correspond to the standard deviation of five consecutive measurements, each averaged over 500 experimental cycles. Examples of the measured ion signals, after subtraction of the TOF mass spectra recorded without the Rydberg excitation laser, but prior to the correction for the v_{Ryd}-dependent amounts of He(n) atoms that make it to the reaction region, are displayed for $v_{Ryd} = 840$ and 1050 m s^{-1} in the insets of Fig. 2. The coloured rectangles in the insets indicate the integration windows used for the three product ions.

This journal is © the Owner Societies 2022

Phys. Chem. Chem. Phys., 2022, **24**, 16360–16373 | **16363**

We do not observe a significant dependence of $I_{CH_{\{1,2,3\}}^+}$ and $I_{CD_{\{1,2,3\}}^+}$ on v_{Ryd} in the range of He(n) velocities probed. The product branching ratios, determined from the mean value and standard deviations of $I_{C(H/D)_{\{1,2,3\}}^+}$ as a function of v_{Ryd} are summarised in Table 2 and compared to the relative branching ratios reported in ref. 40–43 (excluding the contributions from H^+ and D^+ ions, which were not detected in our experiments, and CH_4^+ and CD_4^+, for which we estimate a branching ratio of $\leq 3\%$).

The measured product branching ratios for all product ions in the current work are consistent with those measured in previous work, within the experimental uncertainty.

The $He^+ + CH_4$ and $He^+ + CD_4$ data sets presented in Fig. 2 were obtained under near-identical experimental conditions (e.g., GS-beam stagnation pressure, valve temperature), so that the product yields for the two reactions can be directly compared. In Fig. 2, the detected product-ion signals for the $He^+ + CH_4$ reaction are almost twice higher than those for the $He^+ + CD_4$ reaction. This result is unexpected because the Langevin rate constant of the former reaction, $k_L^{He^+ + CH_4} = 2.048 \times 10^{-15}$ m s^{-1} is only 2.1% higher than the one of the latter, $k_L^{He^+ + CH_4} = 2.006 \times 10^{-15}$ m s^{-1}. To explain this discrepancy, we first considered the possibility that the CD_4 gas, because of its higher mass of 20.067 u, undergoes different expansion dynamics compared to the CH_4 gas (mass 16.043 u) leading to a lower CD_4 density in the supersonic beam. To test this hypothesis, we repeated the experiment with a GS supersonic beam composed of a $\approx 1:1$ mixture of $^{13}CH_4$ (17.035 u) and $^{12}CD_4$ (20.067 u). The use of a mixture of both gases in the supersonic expansion is expected to reduce the differences in the expansion dynamics of the two species. The choice of $^{13}CH_4$ in this experiment ensures that the dominant product ion of each reaction, namely $^{13}CH_2^+$ and $^{12}CD_2^+$, is less contaminated with product ions from other ion–molecule and Penning-ionisation reactions.

Typical TOF mass spectra recorded with the GS beam containing the $^{13}CH_4$–$^{12}CD_4$ gas mixture are displayed in Fig. 3. When the Rydberg-excitation laser is turned on (green trace), many peaks are observed. Because there is usually more than one molecular ion corresponding to a given mass, most of the peaks cannot be unambiguously assigned to a particular molecular ion. The detected peaks in order of increasing time of flight are assigned to: He^+, $^{13}CH^+$ and $^{12}CD^+$, $^{13}CH_2^+$, $^{12}CD_2^+$ and $^{13}CH_3^+$, $^{13}CH_4^+$ and OH^+, $^{12}CD_3^+$ and H_2O^+, $^{12}CD_4^+$, N_2^+, and O_2^+. By subtracting the background spectra recorded with the laser turned off [black trace in Fig. 3], we obtain a time-of-flight spectrum which only contains the ion–molecule reaction products from the two reaction systems [blue trace in Fig. 3]. If the H^+/D^+ product channel is disregarded, the main products of the $He^+ + ^{13}CH_4$ and $He^+ + ^{12}CD_4$ reactions are $^{13}CH^+$ and $^{13}CH_2^+$, and $^{12}CD^+$ and $^{12}CD_2^+$, respectively. The $^{13}CH^+$ and $^{12}CD^+$ products have the same mass number (14) and we cannot determine the individual contributions to the measured signal. The heavier and more dominant reaction product of the $He^+ + ^{13}CH_4$ reaction, $^{13}CH_2^+$, is not contaminated by any other
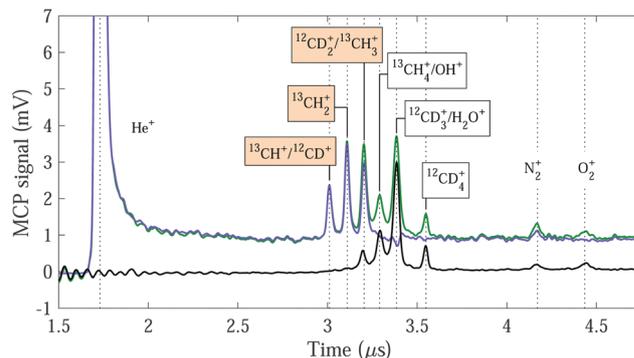

Fig. 3 Measured time-of-flight mass spectra of the products of the reaction between He(n) atoms and methane molecules in a GS beam composed of a $\approx 1:1$ mixture of $^{13}CH_4 : ^{12}CD_4$ (green trace), and background time-of-flight spectrum recorded without the Rydberg-excitation laser (black trace). The blue trace represents the reaction ion products after subtraction of the background signals from Penning ionisation. The coloured boxes indicate the ion products of the $He^+ + ^{13}CH_4$ and $He^+ + ^{12}CD_4$ reactions.

product-ion contributions. The corresponding product ion of the $He^+ + ^{12}CD_4$ reaction, $^{12}CD_2^+$, only coincides in mass with the minor $^{13}CH_3^+$ product of the $He^+ + ^{13}CH_4$ reaction. From our measurements using the pure CH_4 and CD_4 beams, this contribution was determined to be $\sim 11\%$ of the $^{13}CH_2^+$ peak intensity (see Table 2) and can be subtracted to derive the $^{12}CD_2^+$ signal.

The integrated product-ion signals corresponding to the $CH_2^+:CD_2^+$ product-ion ratio, measured with GS beams of pure $^{12}CH_4$ and $^{12}CD_4$ gas in separate experiments and the $^{13}CH_4$–$^{12}CD_4$ mixture, and $v_{Ryd} = 1040$ m s^{-1}, are 0.66 ± 0.04 and 0.72 ± 0.06, respectively. These ratios are identical within the experimental uncertainties, which suggests that the expansion effects do not significantly affect the CH_4/CD_4 densities in the reaction volume. The $He^+ + CH_4$ reaction thus appears to have a larger rate coefficient (by about 40%) at low collision energies than the $He^+ + CD_4$ reaction. This difference is significantly larger than predicted from the Langevin rate coefficients (about 2.1%).

The collision-energy dependence of the total measured product-ion yield (I_{tot}) of the He(n) +CH_4 (purple) and He(n) +CD_4 (green) reactions is displayed in Fig. 4. The triangles and circles indicate measurements with $v_{Ryd} < v_{GS}$ and $v_{Ryd} > v_{GS}$, respectively. The dashed horizontal lines and coloured rectangles represent the mean and standard deviation of the experimentally measured values for I_{tot}. The product yields of these reactions do not exhibit a significant dependence on the collision energy in the $k_B \cdot (0-10)$ K collision-energy range studied experimentally.

In our experiments, there is a very large excess of the ground-state molecules (density ρ_{GS} in the order of 10^{10} cm^{-3} compared to a density ρ_{Rg} of about 10^6 cm^{-3} of the Rydberg atoms). Consequently, the density of the ground-state molecules remains unchanged during the reaction, which corresponds to pseudo-first-order kinetics. In addition, the conditions are such that less than 1% of the Rydberg atoms
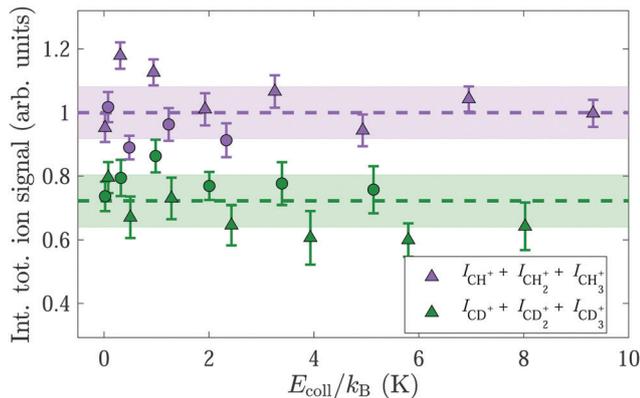
16364 | Phys. Chem. Chem. Phys., 2022, **24**, 16360–16373

This journal is © the Owner Societies 2022

Fig. 4 Total measured product-ion yields of the He$^+$ + CH$_4$ reaction, $I_{CH^+} + I_{CH_2^+} + I_{CH_3^+}$ (purple), and the He$^+$ + CD$_4$ reaction, $I_{CD^+} + I_{CD_2^+} + I_{CD_3^+}$ (green), as a function of the collision energy, $E_{coll} = \mu (v_{Ryd} - v_{GS})^2/2$, in the $k_B \cdot (0-10)$ K range. The triangles (circles) indicate measurements carried out at $v_{Ryd} < v_{GS}$ ($v_{Ryd} > v_{GS}$). The dashed horizontal lines and coloured rectangles represent the mean and standard deviations of each measurement set.

react during the duration Δt of the reaction–observation window. Their concentration therefore also does not significantly change during the reaction and the product yields are proportional to the rate coefficients. Fig. 4 thus indicates that the rate coefficients do not depend on the collision energy, as expected for Langevin-capture reactions. This observation suggests that the charge-octupole interaction between He$^+$ and CH$_4$ (CD$_4$) does not affect the rate coefficients. This aspect is now examined in more detail from a theoretical point of view.

4 The effect of the octupole moment on the rate coefficients of ion–molecule reactions

Because of its tetrahedral symmetry, the methane molecule does not have a permanent electric dipole nor a quadrupole moment. Its first non-vanishing permanent electric moment is the octupole moment. The interaction between the charge of the He$^+$ ion and the octupole moment can lead to a modification of the $R-$ and rotational-state-dependent ion–molecule interaction potentials and capture rate coefficients (R is the distance between the ion and the molecule). In this section, we present a theoretical analysis of this interaction.

We consider methane molecules in their ground electronic ($\tilde{X}$ $^1A_1$) and vibrational state ($v_{1,2,3,4} = 0$). The interaction between the electric field generated by the ion and the octupole moment of the methane molecule results in a mixing of the $|JKM\rangle$ rotational levels and induces a small energy shift from the Stark effect, ΔE_{JKM}, of the rotational energy levels which depends on the distance between the methane molecule and the ion. The total ion–molecule interaction potential, consisting of the pure Langevin term, $V_L(R)$, and the state-dependent Stark shift, ΔE_{JKM}, as described in Article I, is used to calculate the state-dependent capture rate coefficients.

4.1 Nuclear-spin statistics of methane in the T_d (M) group and rotational-state population in the supersonic beam

The methane molecule has a tetrahedral structure and, if tunnelling effects are ignored, its states can be labelled by the irreducible representations A$_1$, A$_2$, E, F$_1$ and F$_2$ of the molecular symmetry group T_d (M). The total wavefunction (including the electronic, nuclear-spin and rovibrational components) must have either A$_1$ or A$_2$ symmetry, both for CH$_4$ and CD$_4$. CH$_4$ (CD$_4$) has three nuclear-spin isomers with total nuclear spin $I = 2, 1, 0$ ($I = 4, 2, 0$). The nuclear spin of 1/2 (1) of the protons (deuterons) in CH$_4$ (CD$_4$) leads to 16 (81) nuclear spin wavefunctions, which span the total irreducible representations:[48–50]

$$\Gamma_{ns}^{CH_4} = 5A_1(I=2) \oplus E(I=0) \oplus 3F_2(I=1) \quad (1)$$

and

$$\Gamma_{ns}^{CD_4} = 15A_1(I=4) \oplus 6E(I=0) \oplus 18F_2(I=2). \quad (2)$$

The allowed rovibronic states span the irreducible representations:

$$\Gamma_{rve}^{CH_4} = 5A_1 \oplus 5A_2 \oplus 2E \oplus 3F_1 \oplus +3F_2 \quad (3)$$

and

$$\Gamma_{rve}^{CD_4} = 15A_1 \oplus 15A_2 \oplus 12E \oplus 18F_1 \oplus +18F_2. \quad (4)$$

The symmetries of the rotational wavefunctions of methane and the nuclear-spin-statistical weights of the rovibronic states determined from the allowed combinations of nuclear-spin and rovibronic wavefunctions are presented in Tables 3 and 4, respectively.

The octupole-allowed transitions in the T$_d$ (M) group are:[51]

$$A_1 \leftrightarrow A_2,$$

$$F_1 \leftrightarrow F_2,$$

Table 3 Symmetry species of the $J = 0-12$ rotational levels of the $^1A_1$ ground state of CH$_4$ and CD$_4$ in the T$_d$ (M) molecular symmetry group (adapted from ref. 48). The last column lists the rotational energies in the ground vibrational state of CH$_4$, neglecting centrifugal distortion terms. The states of A, F and E symmetry are labelled in red, black and blue, respectively (see text for discussion)

J	Γ_{rot}	$E_J = hcB_{CH_4}J(J+1)$
0	A$_1$	0
1	F$_1$	10.4824
2	E $\oplus$ F$_2$	31.4472
3	A$_2 \oplus$ F$_1 \oplus$ F$_2$	62.8944
4	A$_1 \oplus$ E $\oplus$ F$_1 \oplus$ F$_2$	104.824
5	E $\oplus$ 2F$_1 \oplus$ F$_2$	157.236
6	A$_1 \oplus$ A$_2 \oplus$ E $\oplus$ F$_1 \oplus$ 2F$_2$	220.130
7	A$_2 \oplus$ E $\oplus$ 2F$_1 \oplus$ 2F$_2$	293.507
8	A$_1 \oplus$ 2E $\oplus$ 2F$_1 \oplus$ 2F$_2$	377.366
9	A$_1 \oplus$ A$_2 \oplus$ E $\oplus$ 3F$_1 \oplus$ 2F$_2$	471.708
10	A$_1 \oplus$ A$_2 \oplus$ 2E $\oplus$ 2F$_1 \oplus$ 3F$_2$	576.532
11	A$_2 \oplus$ 2E $\oplus$ 3F$_1 \oplus$ 3F$_2$	691.838
12	(A$_1 \oplus$ A$_2 \oplus$ 2E $\oplus$ 3F$_1 \oplus$ 3F$_2$) $\oplus$ A$_1$	817.627

This journal is © the Owner Societies 2022

Phys. Chem. Chem. Phys., 2022, **24**, 16360–16373 | **16365**

Table 4 Nuclear-spin-statistical weights of the rovibronic wavefunctions of CH_4 and CD_4 in the T_d (M) group

CH_4	CD_4	Degeneracy	Total nuclear spin $I(CH_4; CD_4)$
$A_1(5)$	$A_1(15)$	1	$\{2; 4$
$A_2(5)$	$A_2(15)$	1	
E(2)	E(12)	2	0
$F_1(3)$	$F_1(18)$	3	$\{1; 2$
$F_2(3)$	$F_2(18)$	3	

and

$$E \leftrightarrow E,$$

implying that states of symmetry A_1 and A_2, and F_1 and F_2 can interconvert. These transitions are associated with a change of parity and are better described by the complete-nuclear-permutation-inversion group, S_4^*:[52]

$$A_1 \rightarrow A_1^+ + A_2^-,$$

$$A_2 \rightarrow A_2^+ + A_1^-,$$

$$E \rightarrow E^+ + E^-,$$
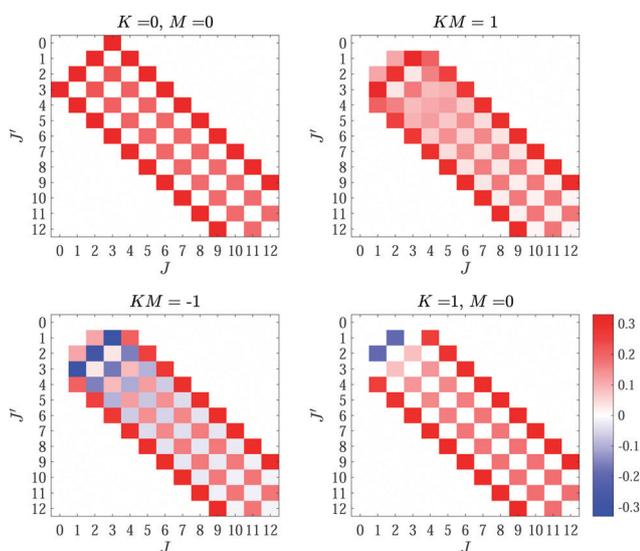
$$F_1 \rightarrow F_1^+ + F_2^-,$$

and

$$F_2 \rightarrow F_2^+ + F_1^-.$$

The selection rules arising from the conservation of the total angular momentum (see eqn (8) in the following section) and of the nuclear-spin symmetry of the rotational wavefunctions of methane in the T_d (M) group are:

$$\Delta J = 0, \pm 1, \pm 2, \pm 3 \quad (0 \not\rightarrow \{0, 1, 2\}; 0 \not\rightarrow 1), \quad (5)$$

$$\Delta K = 0, \quad (6)$$

Fig. 5 Calculated values of the $R-$ independent (without the factor of $e\Omega/(4\pi\varepsilon_0 R^4)$) matrix elements of the Stark Hamiltonian, $\langle J'K'M'|\hat{H}_{Stark}|JKM\rangle$, for the $J = 0$–12 rotational levels of methane and the indicated values of K and M.

and

$$\Delta M = 0. \quad (7)$$

To illustrate these selection rules, the calculated $R-$independent matrix elements [without the factor of $e\Omega/(4\pi\varepsilon_0 R^4)$] of the Stark Hamiltonian in eqn (8) for $J = 0$–12 and KM values of 0 and ± 1 are presented in Fig. 5.

States with $J = 1$ (rovibrational symmetry F_1) and the E component of the $J = 2$ states are metastable because they cannot decay to a lower rotational state without changing the nuclear-spin symmetry (see Table 3). The lowest rotational state that can decay to $J = 0$ is the $J = 3$ state. The ground states of the three nuclear-spin isomers are thus the $J = 0$ (A_1 character), $J = 1$ (F_1 character) and $J = 2$ (E character) states, respectively.

In supersonic expansions of CH_4 and CD_4, states of different nuclear-spin symmetry do not interconvert.[53,54] Because of the relatively large ground-state rotational constant in CH_4 ($B_{CH_4} = 5.241$ cm^{-1}), only the $J = 0$, 1 and 2 states, and thus only the ground state of each nuclear-spin isomer, are significantly populated at the rotational temperature $T_{rot} = 6$ K of our supersonic beam (the fraction of molecules in states with $J > 2$ is $<10^{-5}$). The fraction p_J of CH_4 molecules in state J, including the K and M degeneracies and the nuclear-spin statistical weights, is $p_{J=0}^{CH_4} = 0.31$, $p_{J=1}^{CH_4} = 0.55$ and $p_{J=2}^{CH_4} = 0.14$. The rotational constant of CD_4 is smaller ($B_{CD_4} = 2.591$ cm^{-1}), but the nuclear spin isomers of A and E symmetry still mostly occupy their respective $J = 0$ and $J = 2$ ground states (97.25% and 99.95% of the molecules belonging to the nuclear-spin isomers of A and E symmetry, respectively, are in their respective ground state). The distribution of the nuclear-spin isomer of F symmetry among its three lowest energy states is $\sim 80.5\%$ ($J = 1$), $\sim 18.6\%$ ($J = 2$) and $\sim 0.9\%$ ($J = 3$). The fractions of molecules in specific J states in CD_4 in our supersonic beam ($T_{rot} \approx 6$ K) are: $p_{J=0}^{CD_4} = 0.180$, $p_{J=1}^{CD_4} = 0.537$ and $p_{J=2}^{CD_4} = 0.272$, with $\sim 1\%$ of the molecules in states with $J \geq 3$.

4.2 The interaction potentials between the He$^+$ ion and the methane molecule

In the absence of electric dipole and quadrupole moments, the matrix elements of the Stark Hamiltonian in the basis of the symmetric-top rotational wavefunctions, are given by:[55–57]

$$\left\langle J'K'M' \left| \hat{H}_{Stark} \right| JKM \right\rangle = \frac{e\Omega}{4\pi\varepsilon_0 R^4} \sqrt{(2J'+1)} \sqrt{(2J+1)} (-1)^{K'-M'}$$

$$\times \begin{pmatrix} J & 3 & J' \\ M & 0 & -M' \end{pmatrix} \begin{pmatrix} J & 3 & J' \\ K & 0 & -K' \end{pmatrix}. \quad (8)$$

The He$^+$ + $CH_4(JKM)$ and He$^+$ + $CD_4(JKM)$ interaction potentials

$$V_{int}^{(\ell, JKM)}(R) = -\frac{\alpha' e^2}{8\pi\varepsilon_0 R^4} + \frac{\hbar^2 \ell(\ell+1)}{2\mu R^2} + \Delta E_{JKM}(R)$$

$$= V_L^{(\ell)}(R) + \Delta E_{JKM}(R) \quad (9)$$

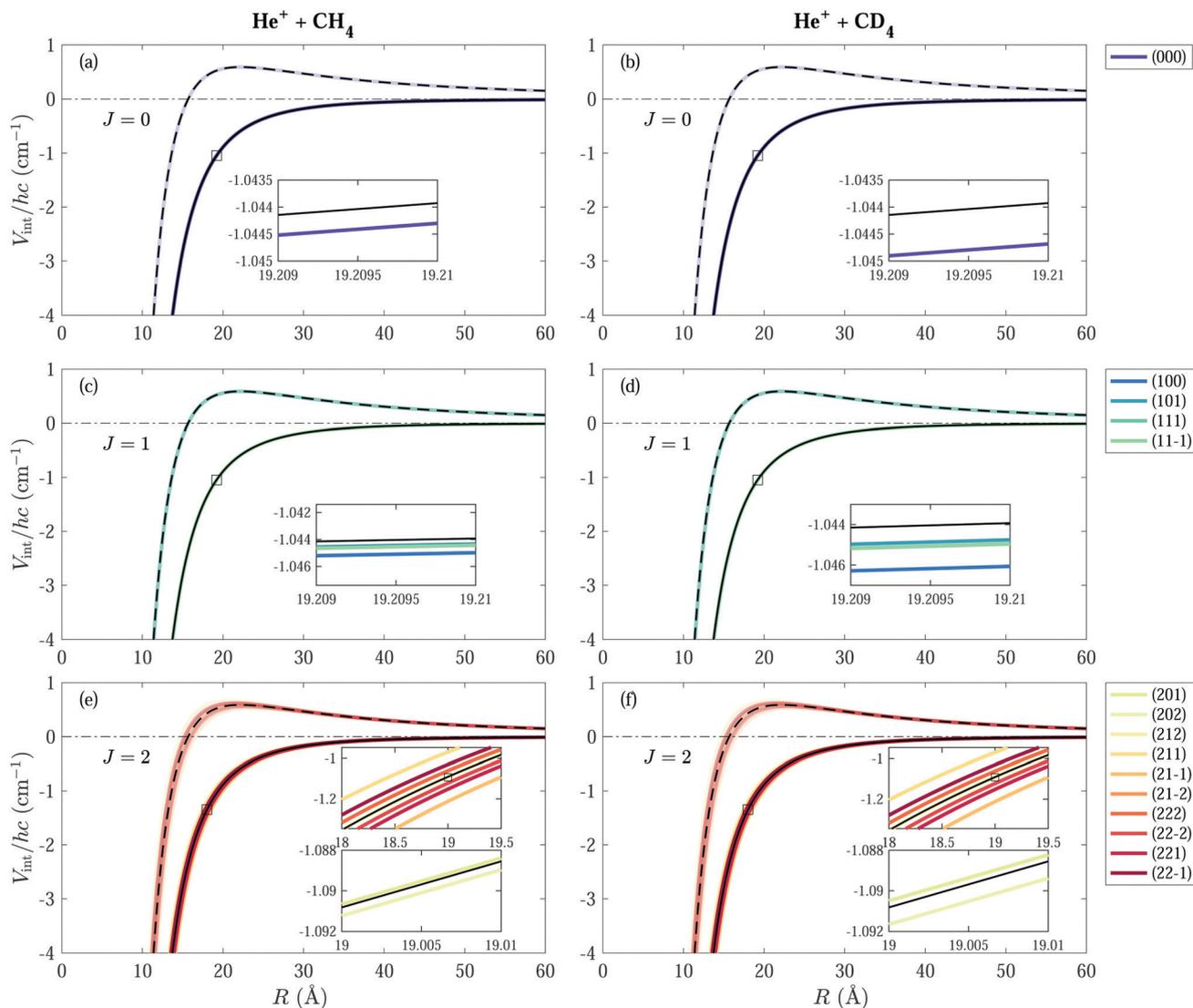**16366** | *Phys. Chem. Chem. Phys.*, 2022, **24**, 16360–16373

This journal is © the Owner Societies 2022

Fig. 6 Calculated interaction potentials between He$^+$ and either CH$_4$[(a), (c) and (e)] or CD$_4$[(b), (d) and (f)], for the $J = 0$, 1 and 2 manifolds of (JKM) states. The solid coloured (transparent coloured) and solid black (dashed black) curves indicate the interaction potential, $V_{int}^{(\ell,JKM)}(R)$, including the effect of the molecular octupole moment (see text for details) and the Langevin interaction potential, $V_L^{(\ell)}(R)$, for $\ell = 0$ ($\ell = 10$), respectively. The legend indicates the state label (JKM).

for rotational levels with $J \leq 2$ are presented in Fig. 6(a)–(f). To determine $\Delta E_{JKM}(R)$, the Stark Hamiltonian was diagonalised for values of R in the 0.1–60 Å range, in steps of 0.075 Å, corresponding to a maximum electric field of $\sim 1.4 \times 10^8$ kV cm^{-1} for the smallest value of R. The rotational constants and octupole moment used in the calculations are B_{CH_4} = 5.241 cm^{-1},[58] B_{CD_4} = 2.591 cm^{-1},[59] and Ω = 3.12 $e\,a_0^3$.[33] Convergence was achieved by including all rotational states with $J \leq 7$.

The solid black (dashed black) and solid coloured (transparent coloured) lines in Fig. 6 indicate the Langevin ion–molecule interaction potential [$V_L^{(\ell)}(R)$] and the total interaction potentials including the charge-octupole interaction [$V_{int}^{(\ell,JKM)}(R)$] for $\ell = 0$ ($\ell = 10$), respectively. For all states, the deviation of $V_{int}^{(\ell,JKM)}(R)$ from $V_L^{(\ell)}(R)$ is very small, particularly for the states of the $J = 0$ and $J = 1$ manifolds. The effect of the octupole moment becomes stronger as J increases from 0 to 2. For states with $J = 0$ and 1, the

effect of the charge-octupole interaction is more pronounced in CD$_4$ than in CH$_4$ because the rotational constant of CD$_4$ is half that of CH$_4$, leading to stronger mixing of the different J levels in the electric field of the He$^+$ ion, as explained below. At an internuclear separation of $R \simeq 19$ Å, which corresponds to the Langevin radius at a collision energy of $\sim k_B \cdot 6.3$ K, the (JKM) = (000) state is shifted from the value of $V_L^{(\ell=0)}$ by ~ -0.0005 cm^{-1} (~ -0.001 cm^{-1}) in CH$_4$ (CD$_4$) [insets of Fig. 6(a) and (b)]. In the $J = 1$ manifold, the potential-energy curves for all (JKM) states are also shifted to lower energies compared to $V_L^{(\ell=0)}(R)$. The change in energy is largest for the (100) state of the $J = 1$ manifold and is ~ 0.001 cm^{-1} (~ 0.002 cm^{-1}) in CH$_4$ (CD$_4$) [insets of Fig. 6(c) and (d)]. This energy shift is twice as large as for the (000) state. In the $J = 2$ manifold of states, the different (JKM) states are shifted to both higher and lower energies compared to $V_L^{(\ell=0)}(R)$ [insets of Fig. 6(e) and (f)]. These shifts are in the order of
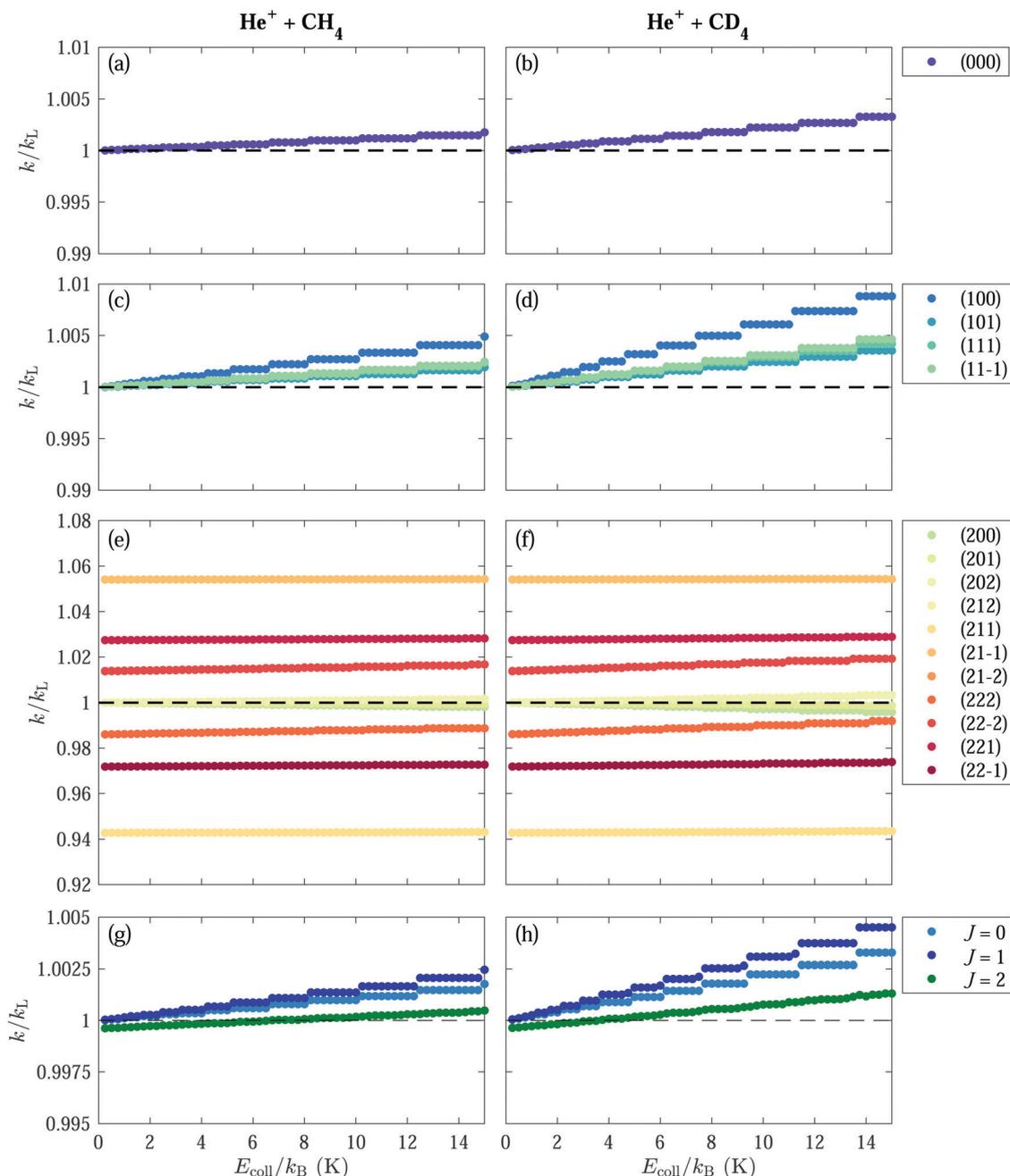
Fig. 7 The calculated rotational-state-dependent rate coefficients $k_i(E_{coll})$ (normalised to k_L) for selected non-degenerate states with $J = 0-2$ for the $He^+ + CH_4$ [(a), (c) and (e)] and $He^+ + CD_4$ [(b), (d) and (f)] reactions, for collision energy in the $k_B \cdot (0.25-15)$ K range. The reaction rate coefficients averaged over all M and K sublevels are displayed in panels (g) and (h).

± 0.15 cm^{-1} in both CH_4 and CD_4. Their larger values come from the fact that these states are closer in energy to states of the $J = 3$ manifold than states with $J = 0$ and 1 and that $J = 3$ states are the lowest rotational levels that can support an octupole moment. In addition, there are more (and stronger) coupling matrix elements to states of the $J = 3$ manifold compared to states with $J = 0$ and $J = 1$, as can be seen by evaluating the relevant Wigner $3 - j$ symbols in eqn (8), see also Fig. 5.

In general, the Stark shifts of all rotational states of CH_4 and CD_4 are several orders of magnitude smaller than the Stark

shifts encountered in polar molecules, such as NH_3[29] and CH_3F[27] (see, *e.g.*, Fig. 6(a) and (b) of Article I) and more than an order of magnitude smaller than the shifts in quadrupolar molecules, such as N_2[32] and H_2[21,32,60] (see, *e.g.*, Fig. 4 and 7 of Article II), as expected.

4.3 The rotational-state-dependent capture rate coefficients

We calculate the state-dependent capture rate coefficients as a function of the collision energy (E_{coll}) by finding the highest classically-allowed partial wave, ℓ_{max}, which results in a

16368 | *Phys. Chem. Chem. Phys.*, 2022, **24**, 16360–16373

This journal is © the Owner Societies 2022

capture, for each selected value of E_{coll}. The value of ℓ_{max} is then used to calculate the maximal impact parameter

$$b_{max} = \hbar \sqrt{\frac{\ell_{max}(\ell_{max} + 1)}{2 E_{coll} \mu}}, \tag{10}$$

the cross section, $\sigma = \pi b_{max}^2$, and the rate coefficients k_i for the methane molecule in state $i = (JKM)$:

$$k_i(E_{coll}) = v_{rel}\sigma = v_{rel}\pi b_{max}^2 = \pi \frac{\hbar^2 \ell_{max}(\ell_{max}+1)}{\sqrt{2\mu^3 E_{coll}}}. \tag{11}$$

The total rate coefficient is obtained by summing over the k_i contributions weighted by the fractional population w_i in state i, determined from the Boltzmann distribution including nuclear-spin-statistical weights:

$$k^{tot}(E_{coll}) = \sum_i w_i \times k_i(E_{coll}). \tag{12}$$

The index i in eqn (12) runs over all (JKM) states that are significantly populated at the rotational temperature of the supersonic beam of 6 K. A total of 81 states were included in the calculation of the total reaction rate coefficients, with $J \leq 3$.

The results of the calculations for the $k_i(E_{coll})$ rate coefficients for the two reactions and rotational states of the $J = 0$, 1 and 2 manifolds are presented in Fig. 7. The calculations were performed in the range of collision energies E_{coll}/k_B between 0.25 and 15 K, in steps of 0.25 K. For states experiencing a total interaction potential that is more (less) attractive than the Langevin potential, the centrifugal potential-energy barrier for a given value of ℓ is lowered (raised) compared to $V_L^{(\ell)}(R)$, leading to values of $k_i(E_{coll})$ that are larger (smaller) than the Langevin rate k_L. The exact dependence of k_i on the collision energy is determined by the Stark shift and the shape of the interaction potential in state i, $V_{int}^{i=(JKM)}(R)$. We can classify the states in three categories as types I, II and III depending on whether the deviation of $k_i(E_{coll})$ from k_L is small ($\lesssim 1\%$), intermediate (~ 1–5%) or large ($\gtrsim 5\%$), respectively, keeping in mind that what we call large here is still small compared to the deviations observed in polar and quadrupolar molecules.

States of type I include all the states from the $J = 0$ and $J = 1$ manifolds [Fig. 6(a)–(d)], the $|M| = 0$, 1, 2 states of the ($J = 2$, $K = 0$) manifold [see lower insets of Fig. 6(e) and (f)] and the $(J, |K|, M) = (2, 2, 0)$ states. At the lowest collision energies, $E_{coll} \simeq k_B \cdot (0.25$–$5)$ K for the He$^+$ + CH$_4$ reaction and $E_{coll} \simeq k_B \cdot (0.25$–$2.5)$ K for the He$^+$ + CD$_4$ reaction, the rate coefficients of these states are very close to the Langevin rate constant, $k_i^{(I)}(E_{coll}) \simeq k_L$. At higher collision energies, the rate coefficients of the type-I states increase (decrease) for interaction potentials that are more (less) attractive than $V_L(R)$. The deviation from k_L in type-I states is more pronounced for CD$_4$ [see Fig. 7(b), (d) and (f)].

States of type II comprise the $|K| = 2$, $|M| = 1$, 2 states from the $J = 2$ manifold. These states experience deviations from $V_L^{(\ell=0)}$ at $R \approx 19$ Å of ~ 0.03–0.06 cm^{-1} [upper insets in Fig. 6(e) and (f)]. The rate coefficients of these states all gradually increase with increasing E_{coll}. The deviation of the rate

coefficients $k_i^{(II)}(E_{coll})$ from k_L is relatively insensitive to the collision energy in the considered range, particularly for the states with $|M| = 1$.

States of type III exhibit the largest deviation from k_L ($\gtrsim 5\%$), but their rate coefficients almost do not depend on the collision energy. States of type III are the $MK = \pm 1$ states of the $J = 2$ manifold, which are shifted by approximately ± 0.15 cm^{-1} from $V_L^{(\ell=0)}(R)$ at $R \approx 19$ Å, in both CH$_4$ and CD$_4$. These states exhibit the largest deviation from $V_L(R)$ [see upper insets in Fig. 6 (e) and (f)] and k_L and have rate coefficients of $\sim 0.94 k_L$ for the $KM = 1$ states and $\sim 1.05 k_L$ for the $KM = -1$ states, in both CH$_4$ and CD$_4$ [see Fig. 7(e) and (f)].

The calculated rate coefficients averaged over all (K, M) sublevels of the $J = 0$, 1 and 2 manifolds are displayed in Fig. 7(g) and (h). They are almost equal to $\sim k_L$ at the lowest collision energy and grow with increasing E_{coll} value. This increase is more pronounced for the $J = 0$ and 1 states. The $J = 2$ manifold consists primarily of states of type II and III. Although the deviations of the interaction potentials from $V_L(R)$ for type-II and III states are the most pronounced, approximately half of the states in this manifold experiences a positive energy shift while the other half experiences a negative energy shift relative to $V_L(R)$. Consequently, the overall effect on the rate coefficient cancels out.

The total capture rate coefficients for the He$^+$ + CH$_4$ and He$^+$ + CD$_4$ reactions obtained after averaging over the rotational-state population of our supersonic beam are displayed in Fig. 8. The weighting factors of each (JKM) sublevel were determined assuming a rotational temperature of the supersonic beam of $T_{rot} = 6$ K and including the nuclear-spin statistical weights. A small increase, of $\sim 0.2\%$ and $\sim 0.4\%$ for CH$_4$ and CD$_4$, respectively, compared to the Langevin rate is predicted in the range of collision energies between 0 and $k_B \cdot$ 15 K. The overall effect of the octupole moment on the total capture rate coefficients arises from states with negative Stark shifts, i.e., mostly from states with $J = 0$ and $J = 1$. The effect is
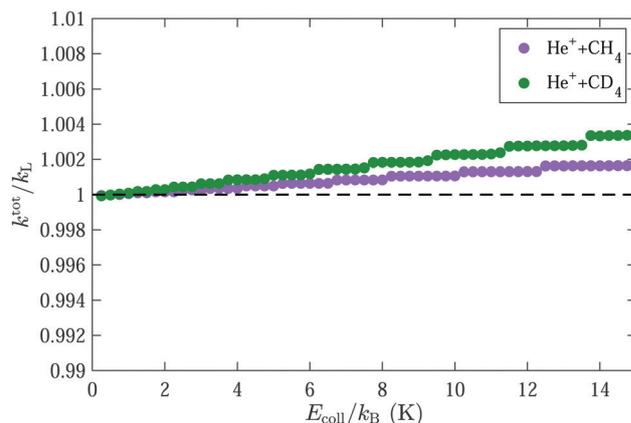
Fig. 8 The calculated collision-energy-dependent total capture rate coefficients for the He$^+$ + CH$_4$ (purple) and He$^+$ + CD$_4$ (green) reactions, normalised to the Langevin rate k_L. The weights for each state are determined assuming a rotational temperature of 6 K and including the nuclear-spin statistical weights.

This journal is © the Owner Societies 2022

Phys. Chem. Chem. Phys., 2022, **24**, 16360–16373 | **16369**

more pronounced in CD_4 than in CH_4 because of the smaller rotational constant of CD_4.

The effect of the octupole moment on the total rate constant is expected to be larger in molecules with larger values of Ω and smaller rotational constants, such as CCl_4.[61] The results presented in Fig. 8 imply that the capture rate coefficients of the $He^+ + CH_4$ and $He^+ + CD_4$ reactions do not significantly depend on the collision energy in the range between 0 and $k_B \cdot 15$ K. This finding is in accord with the experimental observations presented in Fig. 2 and 4, which did not reveal any significant change of the rate coefficient over the range of collision energies probed in the experiment.

5 Conclusions

We have presented measurements of the relative rate coefficients of the reactions between He^+ ions and methane molecules (CH_4 and CD_4) in the collision-energy range between 0 and $\sim k_B \cdot 10$ K. The reactions were studied in a merged Rydberg-He-neutral beam setup, within the orbit of the helium Rydberg electron. We did not observe any dependence of the total product ion yield of either reaction on the collision energy in this range.

The measured product ion yield of the $He^+ + CH_4$ reaction was found to be approximately twice as large as the one of the $He^+ + CD_4$ reaction. This result is unexpected because the Langevin capture rate coefficients of the two reactions are almost identical. Only a very small part of this discrepancy can be explained with the different expansion dynamics affecting the CH_4 and CD_4 supersonic beams, as demonstrated in measurements using a supersonic beam consisting of a $\sim 1:1$ mixture of $^{13}CH_4 : {}^{12}CD_4$. Most likely, the bias towards the product-ion formation in the $He^+ + CH_4$ reaction compared to the $He^+ + CD_4$ reaction arises because of non-adiabatic coupling effects, which are expected to be more pronounced in CH_4 because the protons are lighter than the deuterons.

We have also presented calculations of the rotational-state-dependent capture rate coefficients, which include the effect of the interaction between the charge of the He^+ ion and the octupole moment of the methane molecule. These calculations confirmed that the charge-octupole interaction does not significantly affect the rate coefficients of ion–molecule reactions in the range of collision energies investigated in our studies (i.e., between $k_B \cdot 100$ mK and $k_B \cdot 10$ K). Nevertheless, the calculations revealed small differences, on the order of 5% or less, in the rate coefficients of reactions involving CH_4 and CD_4 in specific rotational states. The effect of these differences might become observable in experiments achieving a higher sensitivity than the present ones or using samples prepared in selected rotational states. The absence of electric dipole and quadrupole moments in CH_4 makes the $He^+ + CH_4$ reaction an attractive system to observe the factor-of-two quantum enhancement of the rate coefficient that has been predicted theoretically for Langevin-type ion–molecule reactions at very low collision energies.[21,62,63] In most other systems, deviations from the Langevin rate constant caused by long-range interactions are dominant and effectively mask the pure quantum enhancement.

This article concludes the three-part series investigating the effects of the molecular multipole moments on the capture rate coefficients of fast, barrierless ion–molecule reactions. In each article, we have presented experimental data on a reaction involving the He^+ ion and a molecule possessing either a permanent dipole, a quadrupole or an octupole moment, and compared the experimental results with calculations of the molecular-rotational-state- and collision-energy-dependent capture rate coefficients. The results overall demonstrate the rapid convergence of the capture rate coefficients to the Langevin rate constant, k_L, as the lowest non-vanishing molecular multipole moment ($n_{mp} = 2^\lambda$) increases in the sequence dipole ($\lambda = 1$), quadrupole ($\lambda = 2$) and octupole ($\lambda = 3$).

In Article I, we presented experimental results and calculations showing the molecular-dipole-moment-induced enhancement of the total reaction rate coefficients of the $He^+ + NH_3$ and $He^+ + ND_3$ reactions, $k^{He^+ + NH_3}$ and $k^{He^+ + ND_3}$, with decreasing collision energy (the ammonia molecule has a dipole moment of 1.47 D).[69] At the lowest experimentally resolvable collision energy of $\sim k_B \cdot 200$ mK, the calculated capture rate coefficients of the two reactions were estimated to be $k^{He^+ + NH_3} \gtrsim 17 k_L$ and $k^{He^+ + ND_3} \gtrsim 22 k_L$.

In Article II, we treated the case of the charge–quadrupole-moment interaction with the example of the $He^+ + N_2$ reaction, demonstrating a suppression of the total reaction rate coefficient, $k^{He^+ + N_2}$, at the lowest collision energies, and an increase of the reaction rate coefficient with increasing energy, reaching a value of $\sim 1.3 k_L$ at $E_{coll}/k_B \approx 10$ K. This suppression at the lowest collision energies was shown to arise from the negative sign of the quadrupole moment of N_2 $\left(Q_{zz}^{N_2} = -1.394 \text{ D Å} \right)$.[70]

In the $He^+ + NH_3/ND_3$ and $He^+ + N_2$ reaction systems, the rate coefficients strongly depend on the rotational level of the molecule. The results we obtained are for jet-cooled samples in which the occupation of rotational levels is approximately described by a rotational temperature of $\sim 6–7$ K. The pronounced deviations we observed at low collision energies are thus the results of the average behaviour of molecules in different rotational states. Much stronger effects could be observed if fully state-selected samples are generated, and if the molecules are aligned or oriented.

The good agreement between the experimentally observed and the calculated state-averaged rate coefficients indicates that the adiabatic capture treatment we used in our calculations, which was developed more than 30 years ago,[17,18] is adequate to describe the energy dependence of the rate coefficients from ~ 50 K down to ≈ 0.1 K, which covers the entire temperature and collision-energy ranges relevant for chemical processes in interstellar clouds.

Capture models do not provide information on the branching ratios for different reaction channels. Moreover, they only provide the absolute values of the capture rate coefficients, whereas our experiments probe the relative rate coefficients for reactive collisions. However, we can use our calculations together with the experimentally measured absolute thermal rate coefficients in previous experiments in order to estimate the absolute thermal coefficients for the studied reactions at

16370 | Phys. Chem. Chem. Phys., 2022, 24, 16360–16373

This journal is © the Owner Societies 2022

Table 5 Overview of the physical properties characterising the reactions between He+ and NH_3, ND_3, N_2, CH_4 and CD_4 investigated in the current article series, and the calculated capture (k_{calc}), measured (k_{obs}) and estimated (k_{est}) thermal rate coefficients at several selected low temperatures relevant for astrophysics

	NH_3	ND_3	N_2	CH_4	CD_4
k_L (10^{-15} m^3 s^{-1})	1.887	1.860	1.637	2.048	2.006
k_{obs} (10^{-15} m^3 s^{-1})	4.5 ($T = 27$ K)[64] 3.0 ($T = 68$ K)[b,29]		1.2^a ($T = 8$ K)[10] 1.3^a ($T = 20$ K)[10]	1.26 ($T = 300$ K)[41]	—
k_{calc} (10^{-15} m^3 s^{-1})	11.3 ($T = 27$ K)[b,29] 7.39 ($T = 68$ K)[b,29]		2.06 ($T = 8$ K)[32] 1.98 ($T = 20$ K)[32]	2.048 (all T)^c	2.006 (all T)^c
k_{est} (10^{-15} m^3 s^{-1})	9.38(0.16) ($T = 3$ K)^b 6.67 (0.12) ($T = 10$ K)^b 9.83(0.17) ($T = 3$ K)^d 7.76 (0.14) ($T = 10$ K)^d		1.28(0.10) ($T = 3$, 10 K)	1.25 (all T)	0.762 (all T)
Estimated percentage of reactive collisions	40% 41%		58 ± 17% 66 ± 20%	61%	37%
Reduced mass μ (u)	3.241	3.336	3.502	3.203	3.337
Polarizability volume α' (10^{-30} m^3)	2.103 (ref. 65)		1.710 (ref. 65)	2.448 (ref. 65)	
Rotational constants (cm^{-1})	9.444 (ref. 66) 6.196 (ref. 66)	5.143 (ref. 67) 3.125 (ref. 67)	1.990 (ref. 68)	5.241 (ref. 58)	2.591 (ref. 59)
Leading multipole moment	Dipole 4.91×10^{-30} C m (ref. 69)		Quadrupole -4.65×10^{-40} C m^2 (ref. 60)	Octupole 7.41×10^{-50} C m^3 (ref. 33)	

^{a} Experimental uncertainty of ±30%. ^{b} Assuming nuclear-spin conservation. ^{c} Current article. ^{d} Assuming nuclear-spin relaxation.

temperatures below ∼100 K, which is the temperature regime relevant for astrophysics.

The thermal rate coefficients calculated using our framework and the experimentally measured absolute rate coefficients at the lowest temperatures available in the literature are listed in Table 5 for the reactions studied in the current series, together with key parameters describing each reaction. For all reactions considered, the calculated thermal rates are higher than the experimentally measured ones, implying that only a fraction of the collisions are reactive. In the case of the reaction between He+ and ammonia, the calculated and experimentally measured thermal rate coefficients at 27 K and 68 K are larger than the Langevin rate k_L by factors of ∼6 and ∼4 (assuming nuclear-spin conservation),[29] and ∼2.4 and ∼1.6, respectively. The enhancement of the He+ + NH_3 thermal reaction rates with decreasing temperature originates from the interaction between the charge of the He+ ion and the dipole moment of the ammonia molecule, as described in Article I. We infer that the fraction of reactive collisions for the He+ + NH_3 reaction is ∼40%. Moreover, our results indicate that the rate coefficient exceeds ∼5k_L at 3 K.

The calculated thermal capture rate coefficients for the reaction between He+ and N_2 at 8 and 20 K are estimated to be ∼26% and ∼21% higher than k_L. The enhancement over the value of k_L of the He+ + N_2 reaction thermal rate coefficient at low temperatures is caused by the interaction between the charge of the He+ ion and the quadrupole moment of N_2, as described in Article II. As the temperature increases, the thermal capture rate coefficient of the He+ + N_2 reaction is expected to converge to the value of k_L. At 50 K and 100 K the thermal capture rate coefficient is 1.16k_L and 1.07k_L, respectively. Using the experimentally measured reaction rate coefficients at 8 and 20 K,[64] we estimate a reaction probability of ∼60% of the He+ + N_2 system, with an uncertainty of ∼±20% resulting from the experimental uncertainty of the measurements.[64]

Because of the minimal effect of the methane octupole moment on the capture rate coefficients of both the He+ + CH_4 and the He+ + CD_4 reactions, the calculated thermal rate coefficients for these reactions already converge to the value of k_L at 1 K. Using (a) the experimentally measured absolute rate coefficients of the He+ + CH_4 reaction available in the literature for 300 K,[41] and (b) the relative product yield of the He+ + CH_4 and He+ + CD_4 reactions measured in our experiments, we estimate that ∼60% and ∼40% of the collisions in the He+ + CH_4 and He+ + CD_4 systems, respectively, are reactive.

Taking the earlier measurements of absolute thermal rate coefficients at elevated temperatures into account and using our calculated capture rate coefficients and the corresponding percentage of reactive collisions, we determined values of the thermal reactive rate coefficients for all reactions in the temperature range relevant for the chemistry of interstellar clouds. Values of these reaction rate constants are given for T = 3 and 10 K in the row labelled k_{est} in Table 5. These values correspond to the sum of the rates of the different reaction channels and the rates for specific channels can be obtained from the respective branching ratios, as given, e.g., in Tables 1 and 2. We recommend that these values be used in kinetic models of the chemical processes in these clouds.

This journal is © the Owner Societies 2022

Phys. Chem. Chem. Phys., 2022, **24**, 16360–16373 | 16371

The reactions between He^+ and CH_4, NH_3 and N_2 involve a charge transfer and thus more than one adiabatic potential-energy surface. These reactions are thus not simply "downhill" reactions on a single surface but involve nonadiabatic dynamics, which is likely to be the reason for the less-than-unity reaction probability. The smaller fraction of reactive collisions in the $He^+ + CD_4$ system compared to the $He^+ + CH_4$ system observed in our study may therefore reflect the fact that protons are lighter than deuterons and thus more likely to undergo nonadiabatic processes. Differences in the zero-point vibrational energies along the reaction paths may also play a role. Capture models do not provide information on the reaction mechanisms leading to different products, nor on the product branching ratios, nor on the percentage of reactive collisions. Nonadiabatic calculations for the reactions studied in this article series would be needed to reach a full understanding of the experimental observations.

Conflicts of interest

There are no conflicts to declare.

Acknowledgements

References

1 T. P. Snow and V. M. Bierbaum, *Annu. Rev. Anal. Chem.*, 2008, **1**, 229.
2 D. Smith, *Chem. Rev.*, 1992, **92**, 1473.
3 I. W. M. Smith, *Annu. Rev. Astron. Astrophys.*, 2011, **49**, 29–66.
4 V. Wakelam, I. W. M. Smith, E. Herbst, J. Troe, W. Geppert, H. Linnartz, K. Öberg, E. Roueff, M. Agúndez, P. Pernot, H. M. Cuppen, J. C. Loison and D. Talbi, *Space Sci. Rev.*, 2010, **156**, 13.
5 E. F. van Dishoeck, *Proc. Int. Astron. Union*, 2017, **13**, 3–22.
6 J. Heimerl, R. Johnsen and M. A. Biondi, *J. Chem. Phys.*, 1969, **51**, 5041–5048.
7 E. Ferguson, F. Fehsenfeld and A. Schmeltekopf, *Adv. At. Mol. Phys.*, Academic Press, 1969, vol. 5, pp. 1–56.
8 D. Smith and N. G. Adams, *Adv. At. Mol. Phys.*, Academic Press, 1988, vol. 24, pp. 1–49.
9 J. K. Kim and W. T. Huntress, *Int. J. Mass Spectrom. Ion Phys.*, 1975, **16**, 451–454.
10 B. Rowe, J. Marquette, G. Dupeyrat and E. Ferguson, *Chem. Phys. Lett.*, 1985, **113**, 403–406.
11 D. Gerlich, *J. Chem. Soc., Faraday Trans.*, 1993, **89**, 2199–2208.
12 C. R. Markus, O. Asvany, T. Salomon, P. C. Schmid, S. Brünken, F. Lipparini, J. Gauss and S. Schlemmer, *Phys. Rev. Lett.*, 2020, **124**, 233401.

13 R. Wester, *J. Phys. B: At., Mol. Opt. Phys.*, 2009, **42**, 154001.
14 S. Willitsch, *Adv. Chem. Phys.*, 2017, **162**, 307–340.
15 B. R. Heazlewood and T. P. Softley, *Nat. Rev. Chem.*, 2021, **5**, 125–140.
16 D. C. Clary, *Mol. Phys.*, 1985, **54**, 605–618.
17 D. C. Clary, *Annu. Rev. Phys. Chem.*, 1990, **41**, 61–90.
18 J. Troe, *Chem. Phys.*, 1987, **87**, 2773–2780.
19 J. Troe, *J. Chem. Phys.*, 1996, **105**, 6249–6262.
20 T. Stoecklin, D. C. Clary and A. Palma, *J. Chem. Soc., Faraday Trans.*, 1992, **88**, 901–908.
21 E. I. Dashevskaya, I. Litvin, E. E. Nikitin and J. Troe, *J. Chem. Phys.*, 2005, **122**, 184311.
22 E. I. Dashevskaya, I. Litvin, E. E. Nikitin and J. Troe, *J. Chem. Phys.*, 2016, **145**, 244315.
23 M. Auzinsh, E. I. Dashevskaya, I. Litvin, E. E. Nikitin and J. Troe, *J. Chem. Phys.*, 2013, **139**, 084311.
24 M. Auzinsh, E. I. Dashevskaya, I. Litvin, E. E. Nikitin and J. Troe, *J. Chem. Phys.*, 2013, **139**, 144315.
25 P. Allmendinger, J. Deiglmayr, O. Schullian, K. Höveler, J. A. Agner, H. Schmutz and F. Merkt, *ChemPhysChem*, 2016, **17**, 3596–3608.
26 P. Allmendinger, J. Deiglmayr, K. Höveler, O. Schullian and F. Merkt, *J. Chem. Phys.*, 2016, **145**, 244316.
27 V. Zhelyazkova, F. B. V. Martins, J. A. Agner, H. Schmutz and F. Merkt, *Phys. Rev. Lett.*, 2020, **125**, 263401.
28 K. Höveler, J. Deiglmayr, J. A. Agner, H. Schmutz and F. Merkt, *Phys. Chem. Chem. Phys.*, 2021, **23**, 2676–2685.
29 V. Zhelyazkova, F. B. V. Martins, J. A. Agner, H. Schmutz and F. Merkt, *Phys. Chem. Chem. Phys.*, 2021, **23**, 21606–21622.
30 F. B. V. Martins, V. Zhelyazkova, Ch. Seiler and F. Merkt, *New J. Phys.*, 2021, **23**, 095011.
31 P. Allmendinger, J. Deiglmayr, J. A. Agner, H. Schmutz and F. Merkt, *Phys. Rev. A: At., Mol., Opt. Phys.*, 2014, **90**, 043403.
32 V. Zhelyazkova, F. B. V. Martins, M. Žeško and F. Merkt, *Phys. Chem. Chem. Phys.*, 2022, **24**, 2843–2858.
33 G. Birnbaum and E. R. Cohen, *J. Chem. Phys.*, 1975, **62**, 3807.
34 B. A. McGuire, *Astrophys. J., Suppl. Ser.*, 2018, **239**, 17.
35 J. H. Lacy, J. S. Carr, N. J. Evans, F. Baas, J. M. Achtermann and J. F. Arens, *Astrophys. J.*, 1991, **376**, 556–560.
36 Y. I. Izotov and T. X. Thuan, *Astrophys. J.*, 2010, **710**, L67–L71.
37 D. Z. Kandula, Ch. Gohle, T. J. Pinkert, W. Ubachs and K. S. E. Eikema, *Phys. Rev. Lett.*, 2010, **105**, 063001.
38 W. A. Chupka and J. Berkowitz, *J. Chem. Phys.*, 1971, **54**, 4256–4259.
39 A. N. Zavilopulo, M. I. Mykyta, A. N. Mylymko and O. B. Shpenik, *Tech. Phys.*, 2013, **58**, 1251–1257.
40 H. Chatham, D. Hils, R. Robertson and A. C. Gallagher, *J. Chem. Phys.*, 1983, **79**, 1301–1311.
41 W. T. Huntress, J. B. Laudenslager and R. F. Pinizzotto, *Int. J. Mass Spectrom. Ion Phys.*, 1974, **13**, 331–341.
42 G. Mauclaire, R. Derai and R. Marx, *Int. J. Mass Spectrom. Ion Phys.*, 1978, **26**, 289–301.
43 N. G. Adams and D. Smith, *J. Phys. B: At. Mol. Phys.*, 1976, **9**, 1439–1451.
44 R. C. Bolden, R. S. Hemsworth, M. J. Shaw and N. D. Twiddy, *J. Phys. B: At. Mol. Phys.*, 1970, **3**, 45–60.

16372 | *Phys. Chem. Chem. Phys.*, 2022, **24**, 16360–16373

This journal is © the Owner Societies 2022

45 K. Motohashi and S. Tsurubuchi, *J. Phys. B: At., Mol. Opt. Phys.*, 2000, **33**, 5215–5224.

46 W. C. Wiley and I. H. McLaren, *Rev. Sci. Instrum.*, 1955, **26**, 1150–1157.

47 M. D. Morse, *Atomic, Molecular, and Optical Physics: Atoms and Molecules*, Academic Press, 1996.

48 P. R. Bunker and P. Jensen, *Molecular Symmetry and Spectroscopy*, NRC Research Press, Ottawa, Canada, 2006.

49 J. T. Hougen, Methane Symmetry Operations, **https://www.nist.gov/pml/methane-symmetry-operations**.

50 Z. Bjelobrk, C. M. Tanner and M. Quack, *Z. Phys. Chem.*, 2015, **229**, 1575–1607.

51 M. Hepp, G. Winnewisser and K. M. Yamada, *J. Mol. Spectrosc.*, 1991, **146**, 181.

52 M. Quack, Fundamental Symmetries and Symmetry Violations from High Resolution Spectroscopy, in *Handbook of High Resolution Spectroscopy*, ed. M. Quack and F. Merkt, Wiley, Chichester, 2011, vol. I.

53 H. J. Wörner, X. Qian and F. Merkt, *J. Chem. Phys.*, 2007, **126**, 144305.

54 G. Wichmann, E. Miloglyadov, G. Seyfang and M. Quack, *Mol. Phys.*, 2020, **118**, e1752946.

55 R. N. Zare, *Angular momentum*, John Wiley & Sons, New York, 1988.

56 S. S. M. Wong, *Introductory Nuclear Physics*, John Wiley & Sons, New York, 1998.

57 A. D. Buckingham, *Q. Rev., Chem. Soc.*, 1959, **13**, 183–214.

58 G. Herzberg, *Molecular spectra and molecular structure; Volume III – Electronic spectra and electronic structure of polyatomic molecules*, Van Nostrand, New York, 1966.

59 H. M. Kaylor and A. H. Nielsen, *J. Chem. Phys.*, 1955, **23**, 2139.

60 E. I. Dashevskaya, I. Litvin, E. E. Nikitin and J. Troe, *J. Chem. Phys.*, 2004, **120**, 9989–9997.

61 S. Brode, C. Kölmel, H. Schiffer and R. Ahlrichs, *Z. Phys. Chem.*, 1987, **155**, 23–28.

62 E. Vogt and G. H. Wannier, *Phys. Rev.*, 1954, **95**, 1190–1198.

63 B. Gao, *Phys. Rev. A: At., Mol., Opt. Phys.*, 2011, **83**, 062712.

64 J. B. Marquette, B. R. Rowe, G. Dupeyrat, G. Poissant and C. Rebrion, *Chem. Phys. Lett.*, 1985, **122**, 431–435.

65 T. N. Olney, N. M. Cann, G. Cooper and C. E. Brion, *Chem. Phys.*, 1998, **223**, 59–98.

66 Š. Urban, R. D'Cunha, R. Romola, K. N. Rao and D. Papoušek, *Can. J. Phys.*, 1984, **62**, 1775–1791.

67 F. Daniel, C. Rist, A. Faure, E. Roueff, M. Gérin, D. C. Lis, P. Hily-Blant, A. Bacmann and L. Wiesenfeld, *Mon. Not. R. Astron. Soc.*, 2016, **457**, 1535–1549.

68 K. P. Huber and G. G. Herzberg, *Molecular spectra and molecular structure; Volume IV – Constants of diatomic molecules*, Van Nostrand Reinhold Company, New York, 1979.

69 M. D. Marshall, K. C. Izgi and J. S. Muenter, *J. Chem. Phys.*, 1997, **107**, 1037–1044.

70 C. Graham, D. A. Imrie and R. E. Raab, *Mol. Phys.*, 1998, **93**, 49–56.

This journal is © the Owner Societies 2022

Phys. Chem. Chem. Phys., 2022, **24**, 16360–16373 | **16373**